Journal of
Applied
Crystallography
ISSN 0021-8898

Received 1 May 2013
Accepted 20 September 2013

Lattice strain distribution resolved by X-ray Bragg-surface diffraction in an Si matrix distorted by embedded $FeSi_2$ nanoparticles

Rossano Lang,[a]* Alan S. de Menezes,[b] Adenilson O. dos Santos,[c] Shay Reboh,[d,e] Eliermes A. Meneses,[f] Livio Amaral[d] and Lisandro P. Cardoso[f]

[a]Instituto de Ciência e Tecnologia – ICT, UNIFESP, São José dos Campos, SP 12231-280, Brazil, [b]Departamento de Física – CCET, Universidade Federal do Maranhão, São Luis, MA 65085-580, Brazil, [c]CCSST, Universidade Federal do Maranhão, Imperatriz, MA 65900-410, Brazil, [d]Programa de Pós-Graduação em Ciências dos Materiais – PGCIMAT, Instituto de Física, UFRGS, Porto Alegre, RS 91501-970, Brazil, [e]Leti – Minatec Campus, CEA, Grenoble 38054, France, and [f]Instituto de Física Gleb Wataghin – IFGW, UNICAMP, Campinas, SP 13083-859, Brazil. Correspondence e-mail: rossano.lang@unifesp.br

Out-of-plane and primarily in-plane lattice strain distributions, along the two perpendicular crystallographic directions on the subsurface of a silicon layer with embedded $FeSi_2$ nanoparticles, were analyzed and resolved as a function of the synchrotron X-ray beam energy by using $\omega{:}\varphi$ mappings of the $(\bar{1}11)$ and (111) Bragg-surface diffraction peaks. The nanoparticles, synthesized by ion-beam-induced epitaxial crystallization of Fe^+-implanted Si(001), were observed to have different orientations and morphologies (sphere- and plate-like nanoparticles) within the implanted/recrystallized region. The results show that the shape of the synthesized material singularly affects the surrounding Si lattice. The lattice strain distribution elucidated by the nonconventional X-ray Bragg-surface diffraction technique clearly exhibits an anisotropic effect, predominantly caused by plate-shaped nanoparticles. This type of refined detection reflects a key application of the method, which could be used to allow discrimination of strains in distorted semiconductor substrate layers.

© 2013 International Union of Crystallography

1. Introduction

The rapid progress in scaling of microelectronics has led to element sizes of subnano order, which has required the development of high-spatial-resolution analytical experimental techniques able to quantitatively evaluate lattice strain distributions at the nanometric scale (Chu *et al.*, 2009). Many intrinsic material properties, including those most significant to silicon-based technology such as band gap, effective mass, mobility, diffusivity and activation of dopants, and oxidation rates, are severely altered by stress/strain effects (Sun *et al.*, 2007; Chidambaram *et al.*, 2006). It has been recognized, therefore, that not only structural defects but also lattice elastic stress/strain near to epilayer/substrate interfaces (for instance, originated by different thermal expansion coefficients) are factors that crucially influence device performance and reliability. In this context, it is of fundamental technological importance to detect and to quantify, with high resolution, in-plane and out-of-plane lattice strain distributions in low-dimensional structures, since an anisotropic strain may, for example, limit or enhance the injection or mobility of charge carriers in one of the **x**, **y** or **z** directions (Baykan *et al.*, 2010). The term 'in-plane' refers to the *xy* plane, while 'out-of-plane' refers to the direction along the *z* axis. On the other hand, in material structures with optical response such as in a silicon waveguide, it has been observed that the presence of an inhomogeneous strain can give rise to the emergence of second-order nonlinear optical phenomena (second-harmonic generation), highly desirable for silicon-based photonics (Cazzanelli *et al.*, 2012).

An approach that appears to be very promising in determining distribution of lattice elastic strain is the X-ray multiple diffraction (XRMD) technique (Chang, 2004). This versatile and high-resolution technique has been developed and successfully applied as a three-dimensional microprobe to study crystalline materials, leading to several interesting contributions regarding semiconducting epitaxial systems in which the lattices of a layer and/or substrate can be investigated separately just by the selection of one appropriate reflection peak (Morelhão *et al.*, 1991, 1998; Sun *et al.*, 2006; Hayashi *et al.*, 1997; Orloski *et al.*, 2005; dos Santos *et al.*, 2009). As the lattice symmetry plays a fundamental role in XRMD, the technique has enough sensitivity to detect subtle lattice distortions in a substrate (or layer) which originate from any symmetry change. Recently, we have reported (Lang *et al.*, 2010) a study on the effects caused by the formation of $FeSi_2$ nanoparticles in the Si lattice by using this technique. In that case, the nanoparticles were synthesized by Fe^+-ion implantation at low dose, followed by the ion-beam-induced epitaxial

crystallization method. We observed the existence of metallic γ-$FeSi_2$ nanoparticles embedded within the implanted/recrystallized Si region, with different orientations and morphologies (sphere and plate shape) and responsible for distinct strains in the Si host lattice.

In this work, out-of-plane and primarily in-plane lattice strains along two different directions (90° apart) on an Si layer distorted by nanoparticles were resolved as a function of the incident synchrotron X-ray beam energy. With further supporting data, lattice parameters and strain distribution were inferred through the analyses of ω:φ mappings of X-ray secondary beams that are diffracted along the sample subsurface, a singular case of the XRMD phenomenon denominated as Bragg-surface diffraction (BSD). The mappings show a prominent anisotropic strain effect in the lattice of the Si layer containing nanoparticles, mostly induced by oriented plate-like nanoparticles. However, this work is not only limited to the strain experimental measurements. We also evaluated by calculation the average path length of an X-ray BSD secondary beam as a function of the Si sample depth as well as of the incident synchrotron X-ray beam energy used in the experiments. We have noticed that BSD secondary beams with different energies are capable of reaching different in-plane regions that have contributed to the strain distribution detected.

2. Experimental details

An *n*-type (001) surface-oriented Czochralski Si wafer (thickness 500 μm, resistivity 10–20 Ω cm) was used as host matrix. Mass-separated Fe^+ ions at an energy of 40 keV were implanted at room temperature at an ion dose of 5×10^{15} cm^{-2}. Channeling effects were avoided by tilting the sample 7° from normal with respect to the incident beam direction. The typical iron beam current density during implantation was about 150 nA cm^{-2}. Subsequently, the Si layer (~90 nm thickness) amorphized by the Fe^+ implantation was recrystallized under high-energy irradiation using a 600 keV Si^+ beam (current density ~1 μA cm^{-2} and a total dose of 6×10^{16} ions cm^{-2}), with the substrate kept at 623 K and without any tilt. This process is known as ion-beam-induced epitaxial crystallization (IBIEC) (Priolo & Rimini, 1990). The dose rate resulting from the Si beam current was 6.2×10^{12} ions cm^{-2} s^{-1}. The sample had not received any post-thermal treatment.

The structures from as-implanted and recrystallized samples were analyzed and characterized by transmission electron microscopy (TEM) observations (JEOL 2010 operating at 200 kV) in cross-sectional samples prepared by ion milling. Conventional measurements of 004 symmetrical high-resolution rocking curves (HRRCs) were performed on a PANalytical X'Pert MRD triple-axis diffractometer using Cu $K\alpha_1$ (1.54056 Å $\simeq$ 8.0536 keV) radiation. For these measurements, the incident beam was conditioned by a four-crystal Ge(220) asymmetric monochromator and the diffracted beam by a three-bounce Ge(220) crystal analyzer. The (002) symmetrical rocking curves (RCs) as well as mappings of the Bragg-surface diffraction reflections using synchrotron radiation, *i.e.* ω:φ coupled scans at the exact multiple diffraction condition, were obtained using a Huber multiaxis diffractometer mounted at the XRD1 station (Brazilian Synchrotron Radiation Facility, LNLS), with incident beam wavelengths of λ = 1.1008 (4), 1.4611 (5), 1.8314 (5) and 2.2016 (7) Å, as defined by using an Si(111) channel-cut monochromator. The minimum step sizes of the ω and φ axes were both 0.0005°. No slits or analyzer crystals were introduced into the diffracted beam path towards the detector.

3. X-ray multiple diffraction

For a more complete understanding of the experimental results that will follow, a brief discussion of the physical aspects of the XRMD technique is presented. The multiple diffraction phenomenon arises when two or more sets of crystallographic planes within a crystal simultaneously satisfy Bragg's law for a certain incident X-ray beam. For this to occur, crystal primary planes parallel to the surface ($h_p k_p l_p$) are adjusted in ω angle to diffract the incident beam (Fig. 1). Under φ azimuthal angle rotation around the primary reciprocal lattice vector, several other secondary ($h_s k_s l_s$) and coupling ($h_p - h_s$ $k_p - k_s$ $l_p - l_s$) planes, both inclined with respect to the crystal surface, can also enter into diffraction

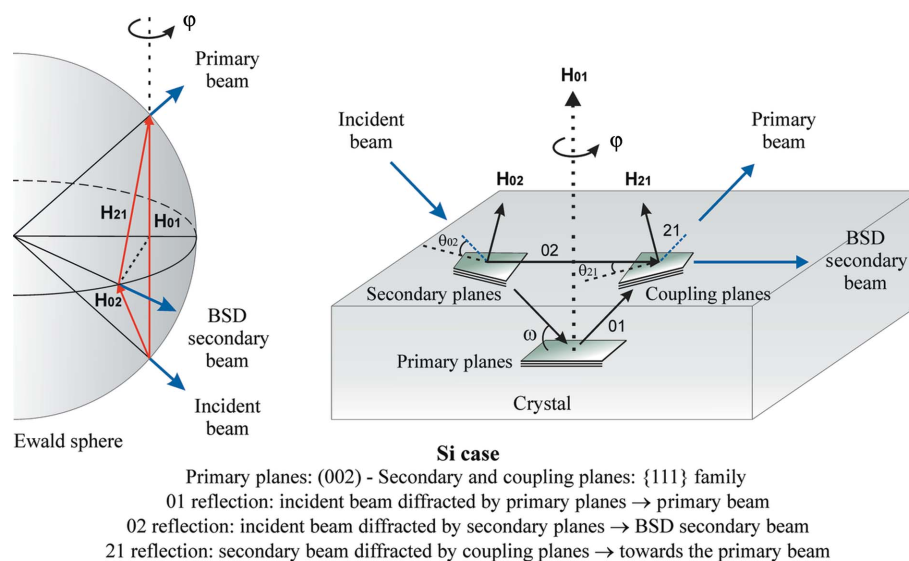

Figure 1
BSD beam representation using the Ewald sphere and the consecutive scattering model scheme with $\mathbf{H}_{01}$ (primary), $\mathbf{H}_{02}$ (secondary) and $\mathbf{H}_{21}$ (coupling) vectors within a crystal. The coupling planes re-scatter the secondary beam towards the primary diffracted beam.

conditions together with the primary planes. The coupling planes provide the interaction between the primary and the secondary reflections and re-scatter the corresponding beams towards the detector. In the pattern of the monitored primary intensity *versus* φ angle, called a Renninger scan (RS) (Renninger, 1937), a series of positive (*Umweganregung*) and negative (*Aufhellung*) secondary peaks appear, symmetrically distributed according to the two symmetry conditions involved: the chosen primary reflection [fourfold in the Si(002) case] and the symmetry plane (twofold). Therefore, several symmetry mirrors are displayed in an RS. The twofold symmetry is established by the two diffraction conditions represented by the entrance and the exit of the secondary reciprocal lattice points from the Ewald sphere under rotation. The position and intensity distribution of these two types of symmetry mirrors are crucial for most of the applications of the technique: for example, to obtain structural information such as lattice parameters, symmetry distortion, misorientation of perfect-crystal regions and mosaicity of the sample (mosaic spread). When a peak in an RS represents an interaction of the incident, primary and secondary diffracted beams, it shows up as a three-beam peak (or three-beam case). However, one can have two or three secondary beams simultaneously interacting to provide four- or five-beam cases (or even cases for $n > 5$ interacting beams), with these secondary beams being either Bragg (reflected) or Laue (transmitted) cases.

Bragg-surface diffraction is a special case of XRMD (Chang, 2004), in which the secondary diffracted beam propagates parallel to the sample surface under an extremely asymmetric geometry. This technique is fundamental for this work. A schematic diagram of the multiple scattering for the BSD case occurring inside the crystal can be seen in Fig. 1, where $\mathbf{H}_{ij}$ are the reciprocal lattice vectors corresponding to the primary planes ($\mathbf{H}_{01}$), secondary planes ($\mathbf{H}_{02}$) and coupling planes ($\mathbf{H}_{21}$). The relationship $\mathbf{H}_{ij} = \mathbf{H}_{0j} - \mathbf{H}_{0i}$ is satisfied for all ij reflections involved in the phenomenon. The secondary beam is generated by the 02 reflection (incident beam diffracted by secondary planes), while the primary beam is originated by the 01 reflection (incident beam diffracted by primary planes) and has its intensity enhanced by the 21 reflection (secondary beam diffracted by coupling planes). These BSD reflections, which appear as peaks in an RS, carry information on the sample surface and even on the interface (layer/substrate) of epitaxial structures (Morelhão *et al.*, 1991; Morelhão & Cardoso, 1993; de Menezes *et al.*, 2010).

Besides the Renninger scan, a method based on the mapping of the exact multiple diffraction condition of the BSD peaks (MBSD or ω:φ mapping), in particular the {111} peak family, has been developed (Morelhão & Cardoso, 1996). This technique can provide information on the crystalline quality and, in principle, on the lattice strain distribution in both the direction perpendicular to the surface (out-of-plane) and the in-plane direction. In this method, the multiple diffraction angular condition is scanned by varying both ω (incidence) and φ (azimuthal) angles, providing a three-dimensional plot of the primary intensity *versus* ω and φ in a coupled way. Through the analysis of the isointensity contours of such plots (two-dimensional projections – ω *versus* φ plane), one can obtain the BSD peak profiles and specific details on the lattice coherence along the beam path and, hence, on the crystalline perfection. For diamond-like crystal structures such as Si, normally one chooses the 002 reflection as the primary reflection instead of 004 for RS measurements and subsequently for ω:φ mappings. Although the 002 reflection is forbidden by the diamond space group, it is utilized at the multiple diffraction condition to allow the observation of all possible secondary contributions as *Umweganregung* peaks. The profile of these peaks is the convolution of the diffraction condition for the secondary and coupling reflections. According to Caticha-Ellis (1969), the profile of a BSD peak in a three-beam case is better defined when the 01 reflection is forbidden by the crystal space group or is very weak in comparison with the 02 and 21 reflections. When a BSD with a forbidden or very weak Bragg reflection is chosen, the diffraction regime (dynamical, kinematical or mixed) depends on the perfect region dimension (block) parallel to the crystal surface (Morelhão & Cardoso, 1996). Under dynamical (kinematical) diffraction, the momentum is transferred by the surface in a primary (secondary) extinction process. If the crystal is ideally imperfect with small perfect diffracting regions (understood here as a mosaic crystal), inter-block diffraction takes place and the kinematical diffraction governs. On the other hand, when the perfect regions become large enough (such as in a quasi-perfect crystal) to allow for intra-block scattering, the dynamical diffraction dominates. In semiconductors, even for ion-implanted ones, intra-block diffraction is generally predominant (Hayashi *et al.*, 1997; Orloski *et al.*, 2005). Summarizing, a Renninger scan of an Si(001) substrate using the Si(002) forbidden reflection will present the ($\bar{1}11$), (111), ($1\bar{1}1$) and ($\bar{1}\bar{1}1$) secondary peaks, which are (i) BSD cases – essential for in-plane studies; (ii) the strongest peaks in the RS – allowing easier identification and indexing; and (iii) fundamental to evaluate lattice parameter distortions along the out-of-plane and in-plane directions through their ω:φ mappings.

4. Results and discussion

Fig. 2 shows representative bright-field TEM observations of the as-implanted and recrystallized samples. Fig, 2(*a*) is a cross-section image (taken at the $[110]_{Si}$ zone axis) of the as-implanted sample, where one observes a ~90 nm-thick amorphous Si–Fe layer produced by the 40 keV Fe^+ implantation and its respective crystal–amorphous interface. This defective intermediate zone between the two distinct regions (crystalline and amorphous) is mainly composed of dangling bonds, and this particular kind of structural defect is the promoter of the IBIEC process (Priolo *et al.*, 1990). Under IBIEC conditions (irradiation + temperature), there is a dynamic rearrangement of these dangling bonds with annihilation in pairs, which promotes a layer-by-layer planar recrystallization toward the surface (Priolo & Rimini, 1990).

The complete recrystallization of the amorphous Si–Fe layer is confirmed by the TEM analyses. A cross-section image of the recrystallized sample, such as shown in Fig. 2(*b*), taken along the $[110]_{Si}$ pole and slightly tilted on the zone axis, reveals an efficient implanted layer regrowth and an impurity redistribution, *i.e.* nanoparticle formation after the IBIEC process. Three regions regarding the nanoparticle distribution are observed: a thin region of a few nanometres thickness, which is closer to the surface (R_1); an Si region (~5 nm) right below the surface with almost no occurrence of nanoparticles (R_2); and a layer (~40 nm wide) with a higher concentration of nanoparticles (R_3). High-resolution TEM (HRTEM) images of the R_1 and R_3 regions are shown in the insets (Figs. 2*c*, 2*d* and 2*e*). In Fig. 2(*c*), it is possible to identify small irregular-shaped nanoparticles at the Si subsurface R_1. Selected-area electron diffraction patterns have indicated that this near-surface layer contains α-$FeSi_2$ nanoparticles (Lang *et al.*, 2010). In the deeper layers (R_2 and R_3), two morphological variants of the metastable γ-$FeSi_2$ phase were observed and recognized: sphere-like nanoparticles epitaxically formed in the substrate with a fully aligned orientation regarding the Si matrix (Fig. 2*d*), and plate-like nanoparticles rotated with respect to the Si matrix (Fig. 2*e*), as previously reported (Lin *et al.*, 1994; Behar *et al.*, 1996). The sphere-like nanoparticles form coherent interfaces with the Si matrix, while the plate-like ones are elongated along the Si$\langle\bar{1}12\rangle$ directions when projected along Si$\langle 110\rangle$. Each plate-shaped nanoparticle is bounded by a pair of coherent interfaces (or semicoherent, in some cases) parallel to Si{111} planes and two incoherent interfaces at the plate edges. These coherent and incoherent interfaces could induce strains in different crystallographic directions. There are four equivalent sets of plate-like nanoparticles parallel to four types of Si{111} plane (Lin *et al.*, 1994). Owing to our TEM-specific conditions of observation, along the $[110]_{Si}$ zone axis, we only detected two sets of elongated plates parallel to Si$(1\bar{1}1)$ and $(\bar{1}11)$. The other two sets of plates, parallel to Si(111) and $(\bar{1}\bar{1}1)$, appear projected as spherical discs and are very similar to spherical nanoparticles and difficult to distinguish from them.

In order to assess the sensitivity of the XRMD technique, we have carried out and compared forbidden 002 rocking curve measurements (ω scan) at the exact multiple diffraction condition for a determined BSD secondary reflection pair using two different X-ray energies. The XRMD peaks used here represent a three-beam simultaneous case (incident, primary and secondary). The results were also compared with conventional HRRC measurements *via* the symmetrical Si(004) reflection. The measurements of the 004 HRRC (using Cu $K\alpha_1 \simeq 8.0536$ keV) on the recrystallized sample and on the pristine Si sample used in the synthesis are shown in Fig. 3 at two perpendicular orientations with respect to the sample surface: $\varphi = 0^\circ$ (Fig. 3*a*) and 90° (Fig. 3*b*). Both patterns (recrystallized sample) present practically the same result, even in a semi-log scale, with two distinct peaks (corresponding to R_2 and R_3 distorted regions) superimposed by a stronger peak originating from the matrix beneath the precipitate layer. These two peaks indicate smaller perpendicular lattice parameters (compressive strain) in relation to that of the matrix.

002 RCs using incident synchrotron X-ray beam energies of 5.6353 and 11.2706 keV were measured at the $(\bar{1}11)$ and (111) BSD reflections (02 reflections; Fig. 1), *i.e.* at two fixed azimuthal angles ($\varphi = -9.01$ and 80.99° and $\varphi = -4.19$ and 85.81°, where the Si bulk peak intensity is maximum). These secondary beams diffracted by the corresponding $(\bar{1}11)$ and (111) planes propagate along the two in-plane perpendicular directions $[\bar{1}10]$ and [110], respectively. The results from pristine Si and recrystallized samples are shown in pairs in

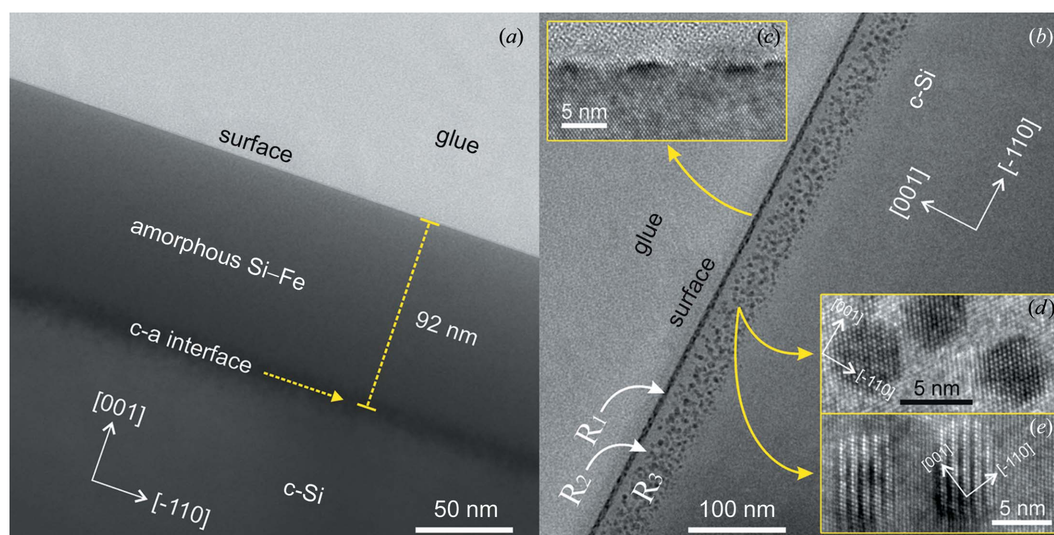

Figure 2
Cross-sectional TEM images of the as-implanted and recrystallized samples obtained along the $[110]_{Si}$ pole. (*a*) Image from the as-implanted sample showing a ~90 nm-thick amorphous Si–Fe layer and its respective crystal–amorphous interface. (*b*) Overview of the recrystallized sample revealing three (R_1, R_2 and R_3) nanoparticle regions at different depths. HRTEM images showing (*c*) irregular shaped α-$FeSi_2$ nanoparticles at the Si subsurface, and (*d*) γ-$FeSi_2$ sphere-like and (*e*) plate-like nanoparticles in a deeper region.

Figs. 3(*c*)/3(*d*) and 3(*e*)/3(*f*), where one can notice striking differences between the 004 and 002 rocking curves on the recrystallized sample. The 002 RC obtained at $\varphi = -9.01^\circ$ (5.6353 keV; Fig. 3*c*) shows three different contributions: a stronger central peak due to the matrix contribution (large perfect regions); a peak (shoulder) at higher angles (compressive strain, also detected by the 004 HRRC) due to convoluted contributions of the R_2 and R_3 regions; and a less intense and broader peak at lower angles (tensile strain), probably associated only with the R_3 region. In contrast, the rocking at $\varphi = 80.99^\circ$ (Fig. 3*d*) exhibits a meaningful profile difference: the lower-angle peak appears more pronounced and closer to the matrix one than in the measurement at $\varphi = -9.01^\circ$, which is a noticeable confirmation of an anisotropic behavior. On increasing the incident X-ray energy to 11.2706 keV (Figs. 3*e* and 3*f*), the peaks related to tensile strain are well resolved.

This lattice strain anisotropy, observed through the difference in the φ angular positions, should be mostly associated with the plate-like nanoparticles and defects in the R_3 distorted region. As mentioned above, the shape of these ordered nanoparticles could introduce different strains in the surrounding Si lattice. Lin *et al.* (1994) reported in detail the shape evolution of individual sphere-like nanoparticles as a function of the annealing temperature, and inferred the transition of the fully aligned orientation (spherical) to the twinned orientation (plate like) with respect to the Si matrix. They concluded that the coarsening rate of the nanoparticles is anisotropic (lengthening rate is considerably greater than thickening) because of the anisotropy of the $FeSi_2$/Si interface coherency. Although there are four equivalent sets of plate-shaped nanoparticles, the ensemble in our recrystallized sample is composed of nanoparticles of different diameters (from 2 to 7 nm), *i.e.* the plates do not have the same length and thickness, which should contribute to the lattice anisotropy measured.

Nonetheless, we cannot rule out the possibility that some recrystallized Si sublayers are also strained, at least those which are underlying the layer containing the nanoparticles. The Si^+-ion irradiation process at high energy (600 keV) with the substrate kept at 623 K promotes the sweep of Fe atoms towards the sample surface and their subsequent precipitation close to the projected range. However, it also produces a high density of point defects and lattice disorder (such as stacking faults, dislocation loops, twinning *etc.*) along the particle track (Jones *et al.*, 1988). Moreover, even under continuous irradiation a significant amount of Fe does not precipitate; the Fe^+ ions diffuse and occupy interstitial sites instead, generating stress/strain in the Si lattice, even though the substrate imposes elastic constraints along the direction parallel to the surface. For the time being, only a qualitative discussion is conducted. Quantitative results will be obtained from ω:φ coupled scans, in which the complete angular information is available.

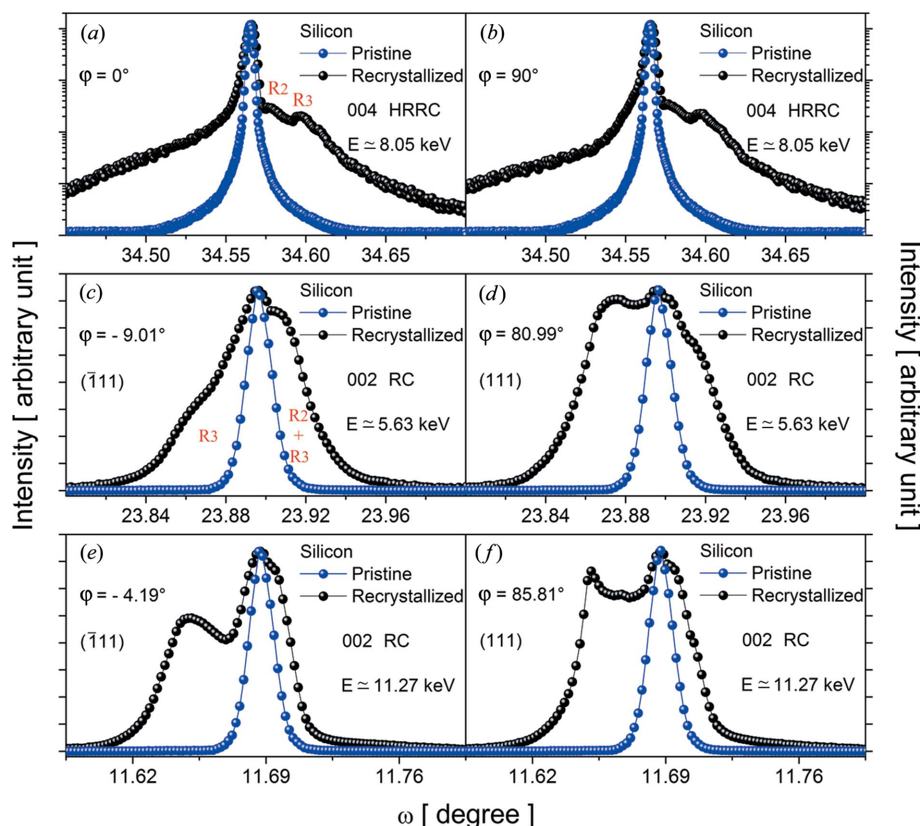

Figure 3
High-resolution rocking curves of the pristine Si and recrystallized samples. The 004 reflection at $\varphi = 0^\circ$ (*a*) and at $\varphi = 90^\circ$ (*b*) for $E \simeq 8.05$ keV. The 002 reflection at the exact condition of two BSD peaks: $\varphi = -9.01^\circ$ (*c*) and $\varphi = 80.99^\circ$ (*d*) for $E \simeq 5.63$ keV, and $\varphi = -4.19^\circ$ (*e*) and $\varphi = 85.81^\circ$ (*f*) for $E \simeq 11.27$ keV.

As the variation of the incident synchrotron X-ray beam energy has changed the 002 RC pattern, it is essential to estimate the average path length (propagation along the surface) of the secondary diffracted beam within the crystal to interpret the experimental data. Hence, the average path length of an X-ray BSD secondary beam was calculated as a function of the incident X-ray beam energy and of the Si sample depth. The average path length (propagation in depth) of the incident beam has also been considered for comparative analysis. The average path length for an incident X-ray beam ($L_{\rm i}$), considering the sample as a plane parallel plate of thickness T, was given by Caticha-Ellis (1969):

$$L_{\rm i} = \frac{1}{2\mu_0} - \frac{T}{\gamma_{\rm i}} \frac{[\exp(-2\mu_0 T/\gamma_{\rm i})]}{[1 - \exp(-2\mu_0 T/\gamma_{\rm i})]}, \qquad (1)$$

where μ_0 is the linear absorption coefficient and $\gamma_{\rm i}$ the direction cosine for the incident beam. An estimate for the average path length of a secondary

diffracted beam (L_s) for a thin layer of thickness T of a semiconductor epitaxial structure has already been obtained (Salles da Costa *et al.*, 1992) as the following equation:

$$L_s = \frac{1}{2\mu_0} - \frac{T}{\gamma}\frac{[\exp(-\mu_0 T/\gamma)]}{[1-\exp(-\mu_0 T/\gamma)]} + \frac{T}{\gamma_i}\frac{[\exp(-2\mu_0 T/\gamma_i)]}{[1-\exp(-2\mu_0 T/\gamma_i)]}, \quad (2)$$

where $1/\gamma = 1/\gamma_i + 1/\gamma_s$ and γ_i (incident) and γ_s (secondary) are the direction cosines determined along their corresponding in-plane directions. The reduced layer thickness (diffracting material volume) that strongly affects the Bragg (reflected) or Laue (transmitted) secondary reflections has been taken into account in that development. However, when the BSD secondary reflections are considered, these special in-plane reflections play the most important role in a Renninger scan of an epitaxial layer. Therefore, the term that contains γ tends to zero because of the BSD beam direction cosine and, in this case, as a first approximation, the average path length for BSD secondary reflections (L_{BSD}) can be given by

$$L_{BSD} = \frac{1}{2\mu_0} + \frac{T}{\gamma_i}\frac{[\exp(-2\mu_0 T/\gamma_i)]}{[1-\exp(-2\mu_0 T/\gamma_i)]}. \quad (3)$$

Note that in the high-thickness limit, equations (1) and (3) assume the value $1/2\mu_0$, which is the bulk case. In turn, in the low-thickness limit (distorted layer range) L_{BSD} is at least one order of magnitude greater than L_i.

Fig. 4 shows the simulated average path length for the incident and BSD beams as a function of the sample depth (T = 0.001–100 µm) for four different X-ray energies (5.6353, 6.7747, 8.4915 and 11.2706 keV). The figure was traced out in an appropriate semi-log scale to strengthen the L_{BSD} behavior close to the surface. The simulation of equation (3) was undertaken for a (111) BSD peak using the Si(002) forbidden reflection as primary reflection. At the Si surface, L_i is virtually zero for all energies, while L_{BSD} presents distinct maximum values. At depths > 1 µm, both average path lengths tend asymptotically to the same value: namely, the corresponding value for the bulk ($1/2\mu_0$ for each energy). In fact, the average path length of a BSD secondary beam (L_{BSD}) as a function of the X-ray energy should be evaluated only at the limit of valid thickness (order of nanometres), since secondary beams occur particularly along the sample surface. The L_i and L_{BSD} values for the surface and for the bulk are displayed in Table 1 for the respective X-ray energies used.

Table 1
Average path lengths of the incident and BSD secondary diffracted beams calculated for the synchrotron X-ray energies used in the experiments.

λ (Å)	Energy (keV)	$L_{i\ (surface)}$ (µm)	$L_{i\ (bulk)}$ (µm)	$L_{BSD\ (surface)}$ (µm)	$L_{BSD\ (bulk)}$ (µm)
2.2016	5.6353	0.0012	12.7476	25.4939	12.7476
1.8314	6.7747	0.0015	21.3355	42.6702	21.3361
1.4611	8.4915	0.0019	40.3951	80.8467	40.4536
1.1008	11.2706	0.0025	91.1194	187.3571	96.2401

The L_i and L_{BSD} average path lengths as a function of X-ray energy evaluated for T = 50 nm are shown in Fig. 5. T = 50 nm corresponds to the thickness of the distorted layer that contains both R_2 and R_3 regions in the recrystallized sample (Fig. 2*a*). For this case, while L_i (propagation in depth) is practically constant, L_{BSD} (propagation along the surface) noticeably increases within the energy range (see log scale). As a result, the BSD beam is able to reach different in-plane regions, which demonstrates how important these reflections are to provide useful information near to and along the sample subsurface.

To evaluate more significantly the strain distribution in the Si lattice distorted by the $FeSi_2$ nanoparticles along both perpendicular and parallel directions, a sequence of ω:φ mappings of the ($\overline{1}$11) and (111) BSD secondary reflections were measured for different X-ray energies (Table 1) as shown

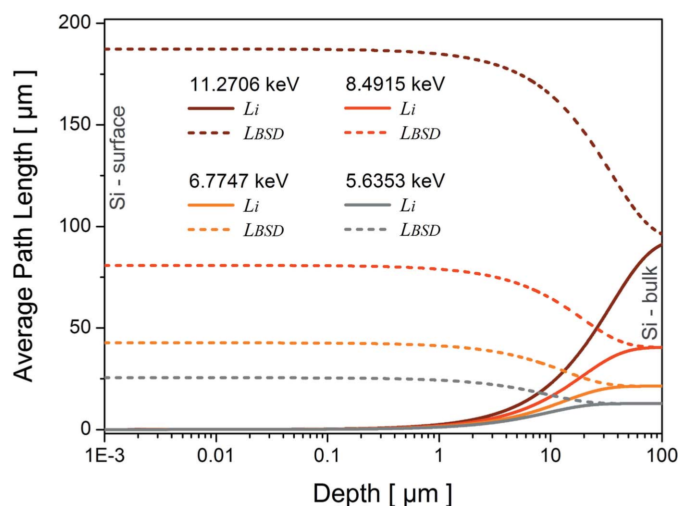

Figure 4
Average path length for the incident and BSD beams obtained as a function of the Si sample depth for four different X-ray energies.

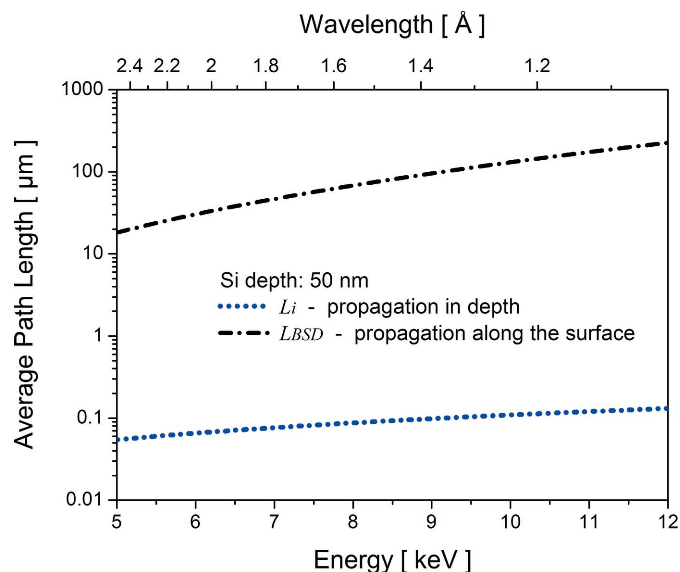

Figure 5
Average path length for the incident and BSD beams obtained as a function of the X-ray energy for a 50 nm fixed depth.

in Fig. 6. These mappings, besides providing an overview on the crystalline perfection of the Si recrystallized layer when compared with the pristine Si, also allow the identification of the regime of diffraction (dynamical, kinematical or mixed) from the isointensity contours. The coupling planes of the $(\bar{1}11)$ and (111) secondary reflections are $(1\bar{1}1)$ and $(\bar{1}\bar{1}1)$, respectively, as can be verified by the condition $\mathbf{H}_{21} = \mathbf{H}_{01} - \mathbf{H}_{02}$. Therefore, these $(\bar{1}11)$ and (111) BSD mappings also provide direct information on the Si$(1\bar{1}1)$ and $(\bar{1}\bar{1}1)$ crystallographic planes, these being parallel to the broad faces of two sets of plate-like nanoparticles. As these planes are in a specific direction, *i.e.* are inclined with respect to the crystal surface, the BSD peak profile can be affected not only by the perfect block dimension but also by the misorientation of blocks perpendicular and parallel to the surface, or even by the slight rotation of diffracting perfect regions.

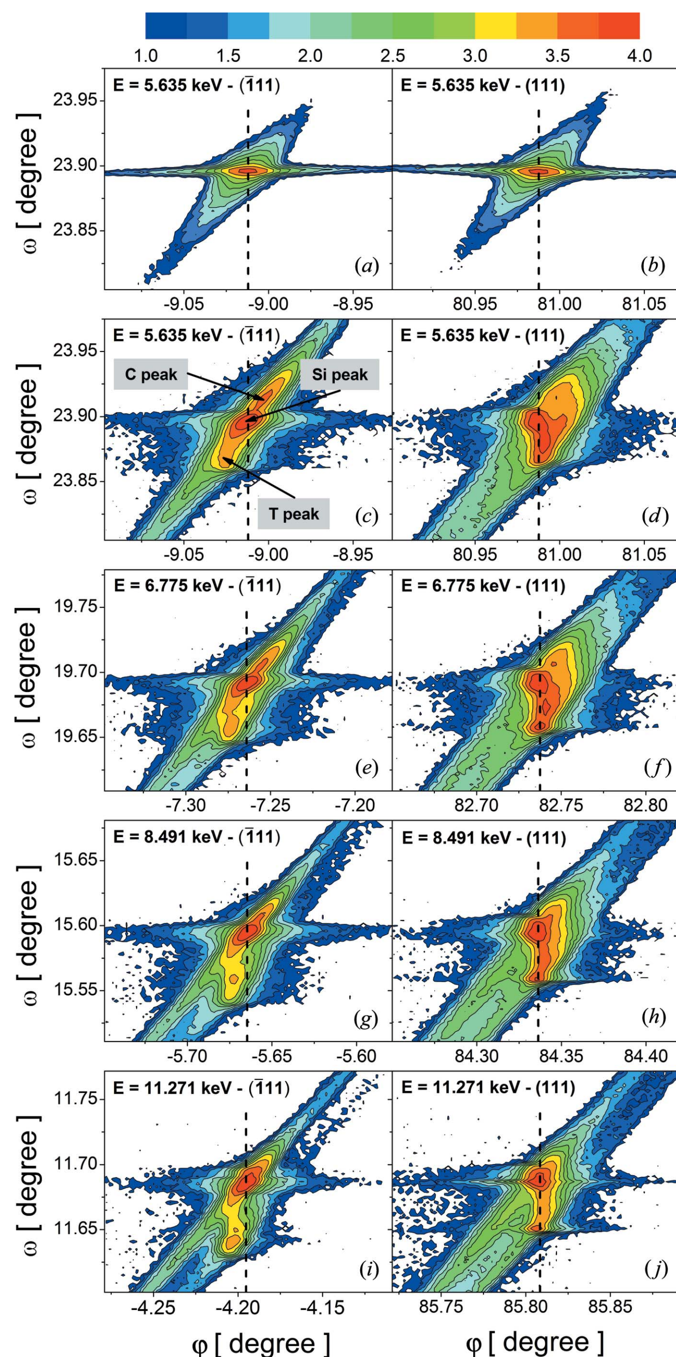

Figure 6
Anisotropic behavior observed on ω:φ mappings of the $(\bar{1}11)$ and (111) BSD secondary reflections for different X-ray energies.

The pristine Si mappings (Figs. 6*a* and 6*b*) for E = 5.6353 keV are also shown for comparison purposes. One observes only a BSD peak at $\omega \simeq 23.89^\circ$ in both $(\bar{1}11)$ and (111) mappings (angular displacement of $\varphi = 90^\circ$), which means that both secondary beams are propagating on the sample subsurface (specifically along the $[\bar{1}10]$ and [110] in-plane directions). Moreover, in these mappings we can observe the main feature of the perfect crystals or nearly perfect crystals such as pristine Si: the intrinsic full width at half-maximum (W) of the peak in the φ scan is larger than that in the ω scan: $W_\varphi >> W_\omega$ (Morelhão & Cardoso, 1996). Such a feature is typical of diffraction under the dynamical regime, *i.e.* when primary extinction is the dominant process in which the momentum is transferred by the surface-detour reflection.

However, the recrystallized sample mappings in Figs. 6(*c*) and 6(*d*) (also for E = 5.6353 keV) clearly show a huge broadening (both ω and φ) of the exact BSD condition (indicated as Si peak) in comparison to the pristine Si, which reflects a reduction of the lattice coherence length (perfect diffracting block dimension). These mappings are examples of superimposed BSD profiles arising from a mixed regime: overlap between the dynamical (scattering within perfect regions) and kinematical (scattering among perfect regions) diffraction. In addition, the intensity contour shapes tend to those expected from a mosaic crystal ($W_\omega > W_\varphi$) (Morelhão & Cardoso, 1996). The kinematical regime occurs significantly as a consequence of the presence of the nanoparticles and of the high density of structural defects remaining after the Si amorphous layer recrystallization process. As mentioned, the recovered Si lattice should still contain a considerable amount of interstitial Fe, which did not precipitate and contributes to the scattering. Other peaks, labeled as C and T, correspond to the compressive and tensile lattice strain contributions, respectively. With reference to Figs. 2 and 3, the C peak is associated with the R_2 and R_3 convoluted regions, while the T peak is related only to the R_3 region. A close inspection of any pair of $(\bar{1}11)$ and (111) BSD peaks reveals a notable anisotropic behavior mainly for the T peak. Although this behavior can be observed in all recrystallized sample mappings, the anisotropy is more pronounced on the higher-energy mappings.

The interpretation of the BSD peaks profile allows quantitative analysis of the lattice parameters of the distinct distorted Si regions. Therefore, elastic strain can be evaluated. Using Bragg's law and the ω angular position of a given peak, it is possible to obtain the perpendicular lattice parameter ($a_\perp$). The parallel lattice parameter ($a_\parallel$) can be obtained by using the calculated $a_\perp$ value, the φ angular position (of the same peak) and the secondary peak position equation (Chang, 2004) given by

$$\cos(\mp\varphi \pm \varphi_0) = \lambda \frac{\left(2a_{\perp}^2 - a_{||}^2\right)}{2a_{\perp}a_{||}\left(2a_{\perp}^2 - 2\lambda^2\right)^{1/2}}, \qquad (4)$$

where the $\mp$ symbol defines the entrance and the exit of the secondary reciprocal lattice point in the Ewald sphere. φ_0 is the angle between $\mathbf{H}_{02\perp}$ (component of $\mathbf{H}_{02}$ on a plane perpendicular to $\mathbf{H}_{01}$) and the reference vector. Here, the ω angular positions of the C and T peaks for each φ azimuthal fixed angle (*i.e.* φ at the maximum intensity of the Si bulk peak according to the X-ray energy value) have been extracted along the dashed lines indicated in Fig. 6. For the lattice strain calculations, the distorted Si and the pristine Si lattice parameters were taken as $\varepsilon = (a_{\rm Si\ distorted} - a_{\rm Si\ bulk})/a_{\rm Si\ bulk}$ to obtain the out-of-plane and in-plane strains induced by the $FeSi_2$ nanoparticles. Fig. 7 shows a plot with all the lattice strains related to C and T peaks as a function of different X-ray energy values (as well as wavelength) used in the experiment. Several interesting features are observed in this figure. The in-plane compressive strain average values are very similar and are approximately zero in both $(\bar{1}11)$ and (111) mappings and remain constant in the entire energy range analyzed, whereas the out-of-plane compressive strain values are rather higher in modulus. Even though the latter presents a slight increase for higher X-ray energies, both compressive strains exhibit isotropy. On the other hand, the out-of-plane and in-plane tensile strains have distinct average values along the $[\bar{1}10]$ and [110] directions, characterizing the anisotropic effect. Moreover, significant increases of the tensile strains are observed as the X-ray energy increases, *i.e.* as a function of the increasing BSD average path length. Finally, it is important to note that even though the variation in propagation depth of the incident beam (from ~0.06 to 0.12 µm, considering a 50 nm distorted Si layer; Fig. 5) in the 5.6353–11.2706 keV energy range is of the same order as the thickness of the Si region that contains the nanoparticles, the incident and primary beams do not contribute directly to the ω:φ mapping features. The primary beam intensity originated by the reflection of the incident beam in the Si(002) primary planes is negligible with respect to the secondary beam intensity diffracted by coupling planes. Actually, this occurs because the Si(002) forbidden reflection was used as primary reflection. On the other hand, the secondary beams propagate along the sample subsurface for up to 187.2 µm (for 11.2706 keV incident beam energy), and their profiles (severely altered by the presence of the $FeSi_2$ nanoparticles and of structural defects) when compared with those of pristine silicon provide the lattice strain distribution in the implanted/recrystallized Si layer.

In summary, the strain effects caused by the $FeSi_2$ nanoparticles in the Si host lattice could only be measured and evaluated at the exact multiple diffraction condition of the $(\bar{1}11)$ and (111) BSD peaks using the Si(002) forbidden reflection as primary reflection, which is only possible under particular extremely asymmetric conditions. This demonstrates all the versatility of the XRMD technique in contrast to the conventional techniques, since with an appropriate choice of the primary reflection one can investigate any crystallographic plane of a crystal.

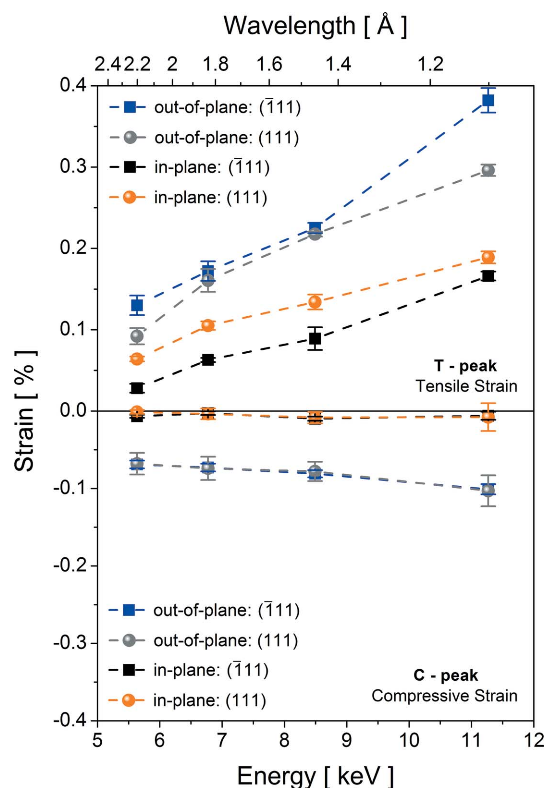

Figure 7
Out-of-plane and in-plane lattice elastic strains induced by $FeSi_2$ nanoparticles as a function of the synchrotron X-ray energy.

5. Conclusion

Out-of-plane and mainly in-plane lattice strain distributions were resolved along the two perpendicular directions $[\bar{1}10]$ and [110] on the subsurface of an Si layer distorted by embedded $FeSi_2$ nanoparticles. Cross-sectional HRTEM images have shown the presence of two kinds of metallic γ-$FeSi_2$ nanoparticles (in the depth range ~50 nm) with different orientations and shapes (sphere and plate like). These nanoparticles together with structural defects are responsible for different strains that were inferred through the ω:φ isointensity contour mappings, plotted as a function of the incident synchrotron X-ray beam energy, at the $(\bar{1}11)$ and (111) exact Bragg-surface diffraction condition. These mappings showed in detail distinct Si regions under compressive and tensile strain. The lattice strain distribution thus elucidated by X-ray Bragg-surface diffraction revealed that the compressive strain component is almost independent of the X-ray energy used, whereas the tensile strain shows a strong dependence on it besides an anisotropic behavior, in both out-of-plane and in-plane directions, predominantly induced by plate-shaped nanoparticles. Furthermore, the average path length (propagation along the surface) of an X-ray BSD secondary beam was calculated as a function of the Si sample depth as well as of the incident synchrotron X-ray beam energy used in the investigation. The results indicate that BSD secondary beams with different energies are capable

of reaching different in-plane regions, enabling us to corroborate the strain distribution detected.

Summing up, the investigation of BSD peak profiles through ω:φ mapping provides a new perspective to analyze crystal surfaces. Finally, we stress the sensitivity, utility and versatility of the presented experimental technique based on X-ray multiple diffraction, since it allows discrimination between the compressive and tensile lattice strain effects in the perpendicular and parallel directions. Both strains were directly detected only when the BSD unique scattering conditions were used appropriately.

The authors would like to thank the Brazilian agencies CNPq, FAPESP and FAPEMA for financial support and the LNLS (XRD1 beamline) staff. SR also acknowledges support from CAPES under process 2358-09-3.

References

Baykan, M. O., Thompson, S. E. & Nishida, T. (2010). *J. Appl. Phys.* **108**, 093716.

Behar, M., Bernas, H., Desimoni, J., Lin, X. W. & Maltez, R. L. (1996). *J. Appl. Phys.* **79**, 752–762.

Caticha-Ellis, S. (1969). *Acta Cryst.* A**25**, 666–673.

Cazzanelli, M., Bianco, F., Borga, E., Pucker, G., Ghulinyan, M., Degoli, E., Luppi, E., Véniard, V., Ossicini, S., Modotto, D., Wabnitz, S., Pierobon, R. & Pavesi, L. (2012). *Nat. Mater.* **11**, 148–154.

Chang, S. L. (2004). *X-ray Multiple-Wave Diffraction: Theory and Applications*, Solid State Sciences Series, Vol. 143. Berlin: Springer-Verlag.

Chidambaram, P., Bowen, C., Chakravarthi, S., Machala, C. & Wise, R. (2006). *IEEE Trans. Electron Devices*, **53**, 944–964.

Chu, M., Sun, Y., Aghoram, U. & Thompson, S. E. (2009). *Annu. Rev. Mater. Res.* **39**, 203–229.

Hayashi, M. A., Avanci, L. H., Cardoso, L. P., Sasaki, J. M., Kretly, L. C. & Chang, S. L. (1997). *Appl. Phys. Lett.* **71**, 2614–2616.

Jones, K. S., Prussin, S. & Weber, E. R. (1988). *Appl. Phys. A Solids Surf.* **45**, 1–34.

Lang, R., de Menezes, A. S., dos Santos, A. O., Reboh, S., Meneses, E. A., Amaral, L. & Cardoso, L. P. (2010). *Cryst. Growth Des.* **10**, 4363–4369.

Lin, X. W., Washburn, J., Liliental-Weber, Z. & Bernas, H. (1994). *J. Appl. Phys.* **75**, 4686–4694.

Menezes, A. S. de, dos Santos, A. O., Almeida, J. M. A., Bortoleto, J. R. R., Cotta, M. A., Morelhão, S. L. & Cardoso, L. P. (2010). *Cryst. Growth Des.* **10**, 3436–3441.

Morelhão, S. L., Avanci, L. H., Hayashi, M. A., Cardoso, L. P. & Collins, S. P. (1998). *Appl. Phys. Lett.* **73**, 2194–2196.

Morelhão, S. L. & Cardoso, L. P. (1993). *J. Appl. Phys.* **73**, 4218–4226.

Morelhão, S. L. & Cardoso, L. P. (1996). *J. Appl. Cryst.* **29**, 446–456.

Morelhão, S. L., Cardoso, L. P., Sasaki, J. M. & de Carvalho, M. M. G. (1991). *J. Appl. Phys.* **70**, 2589–2593.

Orloski, R. V., Pudenzi, M. A. A., Hayashi, M. A., Swart, J. W. & Cardoso, L. P. (2005). *J. Mol. Catal. A Chem.* **228**, 177–182.

Priolo, F. & Rimini, E. (1990). *Mater. Sci. Rep.* **5**, 319–379.

Priolo, F., Spinella, C. & Rimini, E. (1990). *Phys. Rev. B*, **41**, 5235–5242.

Renninger, M. (1937). *Z. Phys. A Hadrons Nucl.* **106**, 141–176.

Salles da Costa, C. A. B., Cardoso, L. P., Mazzocchi, V. L. & Parente, C. B. R. (1992). *J. Appl. Cryst.* **25**, 366–371.

Santos, A. O. dos, Lang, R., de Menezes, A. S., Meneses, E. A., Amaral, L., Reboh, S. & Cardoso, L. P. (2009). *J. Phys. D Appl. Phys.* **42**, 195401.

Sun, W. C., Chang, H. C., Wu, B. K., Chen, Y. R., Chu, C. H., Chang, S. L., Hong, M., Tang, M. T. & Stetsko, Y. P. (2006). *Appl. Phys. Lett.* **89**, 091915.

Sun, Y., Thompson, S. E. & Nishida, T. (2007). *J. Appl. Phys.* **101**, 104503.